A Study Project on Eddy Covariance over Grassland: Leaf Area Index, CO_2 Flux, Evapotranspiration

Linda Adorf, Leonie Bronkalla, Jan Forner, Bettina Haas, Florian Kohler, Felix Lohoff, Nena Raabe, Sophia Schroeder, Timon Stude and Andreas Voigt

Supervised by Otto Klemm and Bastian Paas

Westfälische Wilhelms-Universität Münster - Institute for Landscape Ecology – Climatology Research Group

September 2nd, 2020

Table of Contents

I. Introduction

Exchange processes between biosphere and atmosphere play an important role in the research fields of meteorology, plant physiology and hydrology. Regarding climate change and global warming, as caused especially by CO_2 (Bernstein et al. 2008), a better understanding of the interactions between biosphere and atmosphere is needed. One method for measuring fluxes into and out of an ecosystem is the eddy covariance (EC). It is also supposed to be the most accurate method for this purpose (Burba 2013). However, there are still a lot of uncertainties associated with many measurement methods, especially if it comes to the water vapor flux between ecosystems and the atmosphere. This motivated us to do a comparison of methods.

We collected data during the field work exercise "Biosphere Atmosphere Exchange", which is part of the M. Sc. syllabus "Landscape Ecology" at the University of Münster, Germany. Turbulent fluxes of CO_2, H_2O and sensible heat were measured using the EC method. As a complement, both meteorological and environmental data were collected. Furthermore, we used data to model the evapotranspiration rate using the Penman-Monteith approach. The measurements took place from May 13th until June 8th 2020. We further analysed the data sets towards a deeper understanding of the underlying exchange processes between biosphere and atmosphere.

I.I. Measurement site

The research site is a grassland which is located in vicinity to the Steinfurter Strasse, 3.5 km northwest from the city centre of Münster, Germany. The area under study is bordered by a woody strip in the north, a farm house in the east, another grassland in the south, agricultural cropland in the west, and has a size of 140 m x 60 m. During the period of data collection, the grassland was mowed once, on May 29th. Data recorded after the mowing was discarded from further analysis.

I.II. Workflow

Concentrations of CO_2 and H_2O were measured with a LI-7200 gas analyser (LI-COR, Inc., USA). A three-dimensional sonic anemometer R3-50 (Gill Instruments, Lymington, Hampshire, UK) was used to determine the three-dimensional wind vector as well as the sonic temperature. Measurements were performed with 10 Hz data acquisition frequency. We calculated atmospheric turbulent fluxes with the EC technique using the EddyPro software code, version 7.06 (LI-COR, Inc., USA). Footprint analysis was performed with the model calculation after Kljun et al. (2001), using the data of the wind vector. For this purpose, the software TOVI (Li-Cor 2020) was used.

Furthermore, we determined the Leaf Area Index (LAI) by various methods. The different approaches for the determination were two remote sensing approaches and four types of field measurements (for details Ch. III).

In addition, the potential and current evapotranspiration was calculated using the Penman and Penman-Monteith equations, respectively. Here, the LAI was used as an input variable.

Data handling and evaluation including the creation of diagrams and the calculation of statistics were performed with the R software code (The R Foundation for Statistical Computing 2018) and its script editor RStudio.

II. Footprint

II.I. Data periods and footprint

Two 48-hours periods of continuous westerly winds (wind directions between NW and SW) were selected for further analysis: Period 1 from May 16th, 05:00 hrs to May 18th, 05:00 hrs and period 2 reaching from May 23rd, 05:00 hrs to May 25th, 05:00 hrs, respectively (Fig. 1). All times are given in Central European Time (CET), which is Universal Time Coordinated (UTC) + 1 hour.

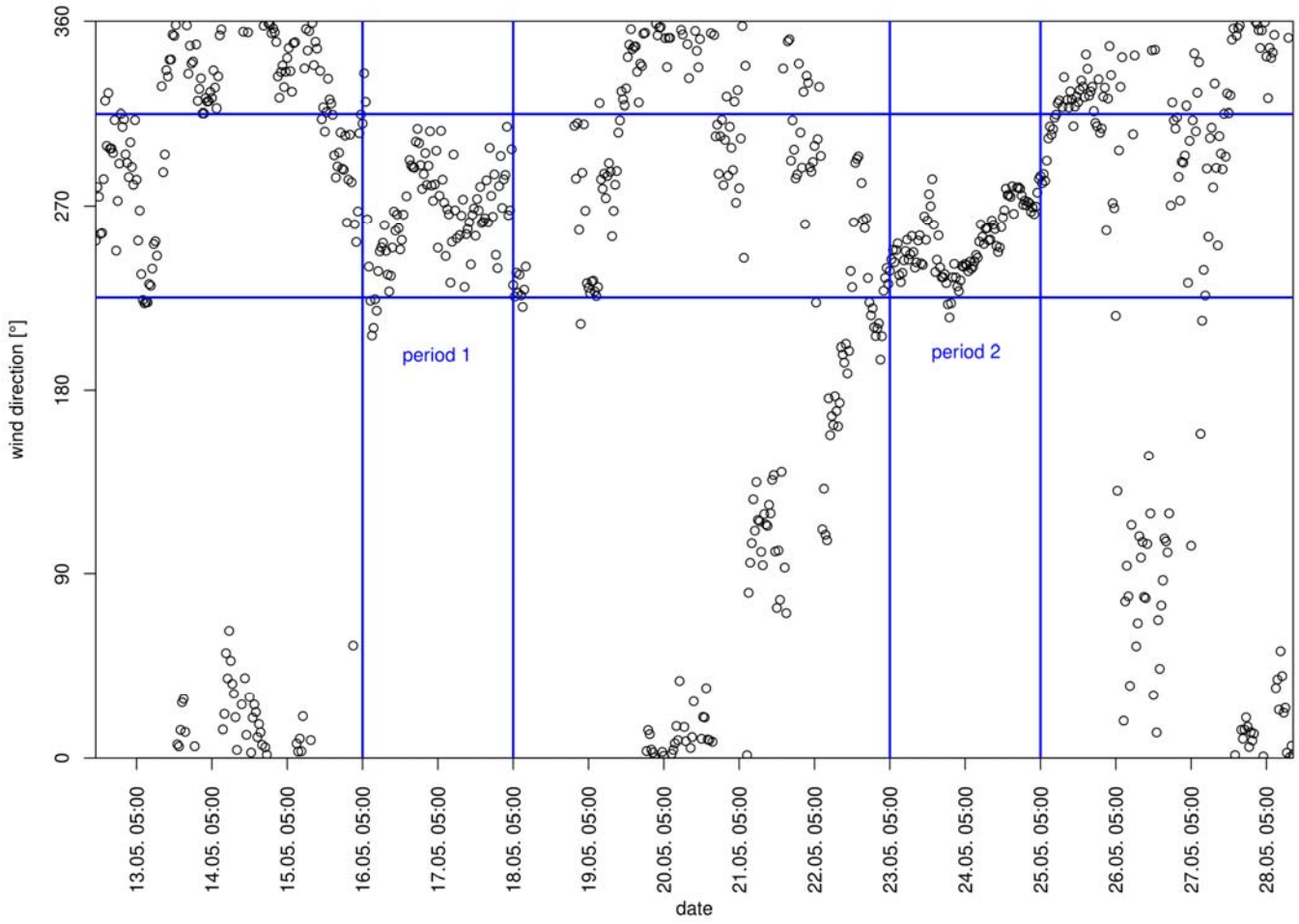

Fig. 1: Wind direction during the experimental phase. Period 1 and period 2 exhibit westerly winds (between NW and SW) throughout and were selected for further analysis

We determined the flux footprints for these periods. A footprint can be defined as 'field of view' (Schmid 2002) as it shows the surface area represented by the eddy covariance data (Finnigan 2004). It is the grassland within the footprint that exhibits the biosphere/atmosphere flux that is eventually measured by the EC setup.

II.II. Methods

Flux data of bad quality (flag 2) was sorted out using the quality-flagging model of Mauder and Foken (2011). Additionally, flux data of CO_2 on May 18th at 00:30 hrs was rejected due to an unusually and prompt high value. This data point had passed the software's quality flagging routine (flag 1), although it is virtually impossible that this peak (factor 26 higher than the preceding and the next data points, respectively, while all other fluxes exhibited no outliers) is valid. The data cleaning resulted in a loss of 47 data points in period 1 and 24 data points in period 2, leaving flux data coverages of over 80 % and 88 %, respectively.

II.III. Results and discussion

For both periods, the high-contribution source area of the footprint is located inside our grassland (green shade) with the highest contribution originating at a distance of about 6 m from the tower (Fig. 2 and Fig. 3). Still, a small amount of data points oversteps the boundary of our grassland, reaching into the adjacent area in the south (period 1 and 2) and in the north (period 1).

Fig. 2: Footprint representing field of view during period 1 (shades representing areas of uniform surface characteristics; Satellite Imagery: Mapbox)

Fig. 3: Footprint representing field of view during period 2 (shades representing areas of uniform surface characteristics; Satellite Imagery: Mapbox)

Our EC setup was installed at 2 m above ground. Although we had mainly low wind speeds during the measurement period, our footprints (high-contribution source areas) were confined to a rather small region around the tower. The footprint thus covers only a small part of the grassland under study. At the same wind speeds, a higher setup would cover a larger footprint area so that the flux data would better represent the characteristics of the entire grassland. At higher wind speeds, the footprints would have been even smaller. We therefore propose to use a higher setup (e.g., 3.5 m above ground) for future measurement setups at the same location.

When analysing a footprint with TOVI, there is the option to use data from a so-called "quality flagging region". This region flags data that may be excluded from further analysis because the respective data quality is not sufficient or because the respective areas are not of interest for the actual study (e.g., different surface characteristics such as water bodies). We decided to not cut out data from those flagged areas because these two areas represent a wood strip (red shade in Figs. 2 and 3) and another grassland (yellow shade) that would likely provide flux data similar to the grassland.

III. Leaf Area Index

The leaf area index (LAI) is defined as the projected area of live green leaves per unit of ground surface (Fang et al. 2013)It is an important variable in the context of plant physiology as well as land surface atmosphere interactions, especially energy, water, and carbon fluxes (Burrows et al. 2002). The LAI is defined by the following formula:

$$\boldsymbol{Eq.1}: \quad \boldsymbol{LAI} = \frac{\boldsymbol{projected\ leaf\ area}\ [\boldsymbol{m^2}]}{\boldsymbol{ground\ area}\ [\boldsymbol{m^2}]}$$

The LAI is a proxy for the photosynthetically active surface (Eugster 2010).

III.I. Remote Sensing

We employed both satellite data and drone data to derive the LAI using two different ways to calculate the LAI:

$$\boldsymbol{Eq.2}: \quad \boldsymbol{NDVI} = \frac{\boldsymbol{NIR} - \boldsymbol{red}}{\boldsymbol{NIR} + \boldsymbol{red}}$$

$$\boldsymbol{Eq.3}: \quad \boldsymbol{LAI_{CALC1}} = \boldsymbol{0.128}^{\frac{\boldsymbol{NDVI}}{\boldsymbol{0.311}}}$$

$$\boldsymbol{Eq.4}: \quad \boldsymbol{LAI_{CALC2}} = \boldsymbol{5.405} * \frac{\boldsymbol{rededge1} - \boldsymbol{rededge2}}{\boldsymbol{rededge1} + \boldsymbol{rededge2}} - \boldsymbol{0.114}$$

The formula of LAI_{CALC1} was proposed by (Fan et al. 2009). It was used in Mongolia and employs only the normalized difference vegetation index (NDVI), with is a commonly used index.

The LAI_{CALC2} formula was created by (Pasqualotto et al. 2019) specially for the Sentinel 2 satellite (Sentinel 2). The respective validation was made in Italy and the formula requires the specific Sentinel 2 two red-edge vegetation bands.

III.I.I Satellite

The resolution of the Sentinel 2 satellite is 10 m x 10 m (Band 1 - 4) and 20 m x 20 m (Band 5 - 8), respectively. The cloud-free images are from May 19th. The satellite images were cropped to the footprint shape (Fig. 4).

Tab. 1: Sentinel 2 Band settings

Band No	Function	Central Wavelength [nm]	Resolution [m]
4	red	665	10
5	Vegetation red-edge I	705	20
8	Near infrared (NIR)	842	10
8a	Vegetation red-edge II	865	20

Based on the two formulas we arrive at these LAIs:

$$Eq.5: \quad LAI_{RS1} = 0.128^{(\frac{B8-B4}{B8+B4}/0.311)}$$

$$Eq.6: \quad LAI_{RS2} = 5.405 * \frac{B8a - B5}{B8a + B5} - 0.114$$

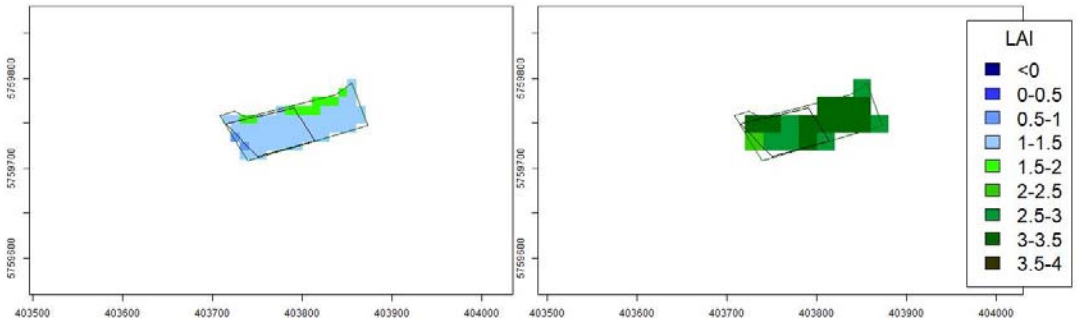

Fig. 4: LAI as analysed from the satellite data. The green line represents the study area and the black line represents the area we chose for the drone flight. Both LAIs are displayed, LAI_{RS1} (left) and LAI_{RS2} (right)

III.I.II Drone

The Wingstra drone with a Micasense camera has a resolution of 0.1 m x 0.1 m. The orthomosaic photo was processed with the Agisoft Metashape Professional software (Fig. 5).

Tab. 2: Band settings Micasense camera

Band No.	Function	Central Wavelength [nm]	Resolution [m]
3	red	668	0.1
4	Near infrared (NIR)	842	0.1
5	Vegetation red-edge	717	0.1

Due to the missing second vegetation red-edge band, we used the bands with the nearest wavelengths for LAI_{UAV2}:

$$\boldsymbol{Eq.7}: \quad \boldsymbol{LAI_{UAV1} = 0.128^{(\frac{B4-B3}{B4+B3}/0.311)}}$$

$$\boldsymbol{Eq.8}: \quad \boldsymbol{LAI_{UAV2} = 5.405 * \frac{B4-B5}{B4+B5} - 0.114}$$

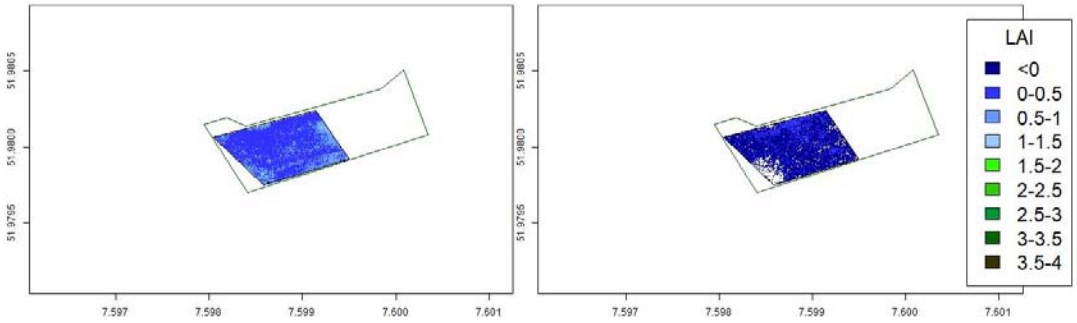

Fig. 5: LAI as analysed from the drone data. The green line represents the study area and the black line represents the area of the drone data. Both LAIs are displayed, LAI_{UAV1} (left), LAI_{UAV2} (right)

III.I.III Results and Discussion

The results of the LAIs differ significantly (Tab. 3). Only LAI_{RS2} is plausible in comparison with literature data. The values of the drone data and the LAI_{CALC2} for the sentinel 2 data are very low. The LAI_{CALC2} was made for a different vegetation type, so it' s use may be restricted to semi-arid regions. For the LAI_{UAV2}, we used the nearest wavelength band, so the LAI_{CALC2} is probably only useful with the exact wavelength of the two vegetation red-edge bands of the sentinel 2 satellites. The LAI_{RS2} of the footprint area and the drone area do not vary significantly. That indicates a homogeneous vegetation on the grassland.

Tab. 3: Mean LAIs and the standard deviation (SD) of the drone and satellite data for the footprint area and drone area, respectively. NAN means not available number

Index	Footprint area mean	Footprint area SD	Drone area mean	Drone area SD
LAI_{RS1}	1.34	0.17	1.27	0.14
LAI_{RS2}	3.02	0.20	3.00	0.11
LAI_{UAV1}	NAN	NAN	0.41	0.26
LAI_{UAV2}	NAN	NAN	-0.20	0.28

III.II. Field Measurements

III.II.I. Direct harvesting technique

One of the methods to quantify the LAI is the direct harvesting technique, which determines the projected leaf area of a given vegetation sample. This is done graphically by calculating the number of coloured pixels of a photograph indicated by the leaves of vegetation compared to a known area (Jurik et al. 1985).

For this purpose, we determined a spot in the grassland, which seemed representative for the measurement area. Within an area of 20 cm x 20 cm the entire vegetation was collected. Subsequently, the vegetation was dried off and glued on white paper. In the following, a high-resolution digital photograph was taken (Fig. 6). The number of coloured pixels of the photograph were calculated using ArcGIS, Version 10.4 (ESRI Inc., Redlands, CA, USA). These were divided by the total amount of pixels (see Eq. 9).

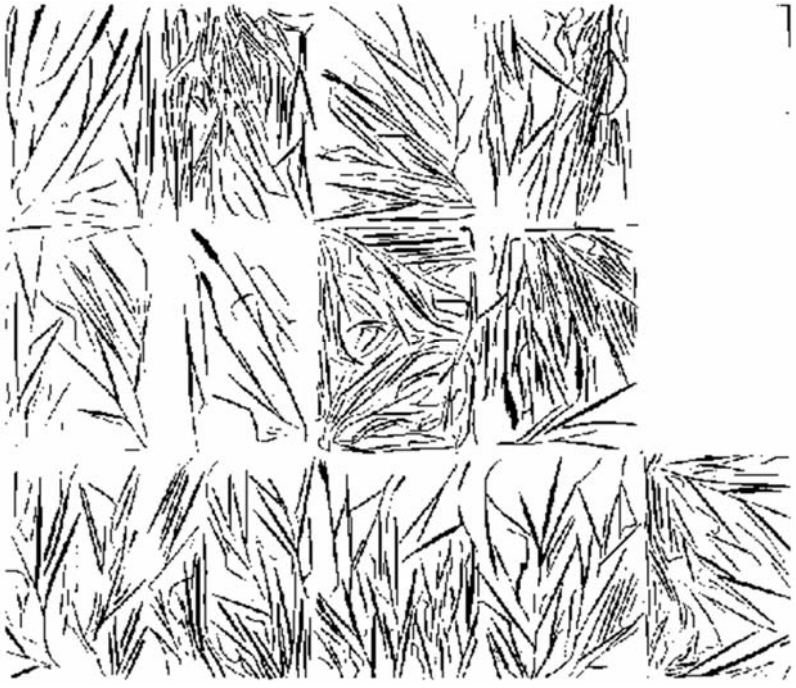

Fig. 6: Photograph which was used for the direct harvesting technique to determine LAI

$$\textbf{Eq. 9:} \quad LAI = \frac{\frac{coloured\ (pixel)}{totalamount\ (pixel)} * areapaper\ [m^2]}{areafield\ [m^2]}$$

The result was multiplicated with the known size of white paper (see Eq. 10).

$$\textbf{Eq. 10:} \quad Size\ of\ Paper = 0.1563\ [m^2] * 1.8585\ [m^2] = 0.2905\ [m^2]$$

The procedure was repeated after exclusion of the inflorescences from the optical analysis (LAI_{DHT}). Again, the number of coloured pixels were divided by the total amount of pixels (see Eq. 11).

$$\textbf{Eq. 11:} \quad LAI = \frac{\frac{757.452}{8.308.439} * 1.8585\ [m^2]}{0.04\ [m^2]} = 4.24$$

A potential source of error lies in the fact that some leaves were not glued perfectly flat onto the white paper. In addition, there was a little amount of shade, which influenced the number of coloured pixels. The analysis of the photograph was difficult since it was not taken from an exact vertical angle. Note that we decided to remove the inflorescences which had a massive impact on the result. This result is more likely to be correct in comparison to literature data (Eugster 2010).

III.III. Field Measurements via Instruments

On June 7th, the LAI was determined with three different methods. Ten individual measuring points were selected. The measuring points were selected in order to best represent all types of vegetation that are present within the measuring field. Locations featuring different vegetation heights were probed. In Fig. 7, the three different measuring instruments are shown.

Fig. 7: Photographs of the three methods to measure the LAI with field instrumentation: A) SunScan S11, B) LAI-2200C, C) Pyranometer (type CMP3)

III.III.I. SunScan S11

The Plant Canopy Analyzer SunScan S11 (Delta-T Devices, Burwell, England) probe consists of 64 photosynthetically active radiation (PAR) sensors embedded in a 1 m long probe. Whenever a reading is taken, all PAR sensors are scanned. The measurements are sent to a control unit. To obtain the LAI, the probe takes a reading above the vegetation as a reference value. Another reading is taken while the probe is pushed as deep under the vegetation as possible. Using the SunScan S11, an average LAI_{S11} of 3.56 ± 0.35 was determined.

III.III.II. LI-COR 2200C

The Plant Canopy Analyzer LAI-2200C (LI-COR Biosciences GmbH, Bad Homburg, Germany) works without additional data or processing and provides instant values on its display. The PCA measures the diffuse radiation to determine the LAI. This means that it measures transmission once under the vegetation and once above the vegetation as a reference value. The reversal of the gap requires images taken at several zenith angles. To achieve this in a single process, LAI meters from LI-COR are equipped with a fisheye lens. The sensor consists of five concentric silicon rings for light detection of the respective five concentric celestial sectors (Danner et al. 2015). For the measurements with the LAI-2200C, the LAI_{LIC} provided an average value of 3.54 ± 0.35.

III.III.III. Pyranometer

The following determination of the LAI is following the approach of (Eugster 2010). The light absorption in a stock can be described with the following exponential model (see Eq. 12) that describes the intensity of the radiation over the vegetation at a certain distance:

$$\boldsymbol{Eq.\,12}: \quad \boldsymbol{I = I_0 * e^{\kappa * LAI}}$$

Values of I was recorded by a pyranometer, type CNR4 (Kipp & Zonen, Delft, The Netherlands), installed 1.5 m above ground. The value I_0 describes the intensity of radiation within the vegetation. For this purpose, another pyranometer, type CMP3 (Kipp & Zonen, Delft, The Netherlands), was placed in the vegetation.

The parameter κ describes a coefficient, which depends on the basic orientation of the leaves in the vegetation. Following Eugster (2010), a value between 0.5 and 0.7 was assumed for a mixed stock with many grasses, but different species and growth heights.

Using the pyranometer approach with a coefficient κ of 0.5, an average LAI_{P05} of 0.92 was calculated. Different LAIs using different coefficients κ calculated with the pyranometer approach are listed in Tab. 4.

Tab. 4: Calculated LAI-Values with different extinction coefficients

Name	Extinction coefficient κ	LAI-Value
LAI_{P05}	0.5	0.92
LAI_{P06}	0.6	0.77
LAI_{P07}	0.7	0.66

III.III.IV. Discussion

We compared different methods to determine the LAI of our grassland under investigation. For smaller areas, methods like the direct harvesting technique are most suitable. The LAI of areas bigger than 20 m x 20 m should be measured with remote sensing, whenever possible with data from the Sentinel 2 satellite which has a resolution of 10 m x 10 m.

The direct harvesting technique is probably the most accurate method because it is a direct method leading to highly accurate data. However, it is also very time-consuming and therefore only suitable for small areas. Whenever a large area under study exhibits a heterogenous vegetation cover (e.g., through varying soil conditions, humidity, land use), several plots need to be harvested for direct LAI measurement and the data needs to be upscaled. This is not only time-consuming, but also introduces considerable uncertainty.

LAI data taken with either the SunScan S11 or the LI-COR 2200C are also very accurate and close to the reference value (Eugster 2010). Those methods are less time-consuming than the direct harvesting method and they can represent bigger areas with much less effort. We think of these approaches to be best suitable for the *in situ* determination of LAI in future projects.

The LAI detected with the Pyranometer shows a lower value (LAI_{P05} = 0.92) as compared to the methods discussed above (LAI_{DHT}, LAI_{S11}, LAI_{LIC}). It remains unclear so far what the potential causes of the disagreement are. We recommend for future investigations on this topic to install several pyranometers into the understory of the vegetation in order to monitor the LAI continuously over the entire measuring period.

Mostly, the LAIs as determined with various methods are quite similar to each other. The LAI_{DHT} is somewhat above the LAI_{S11} and LAI_{LIC}, which can likely be explained by the fact that these two methods are using mean values. The spot that was selected in the grassland for the direct harvesting technique may have had more vegetation and thus a higher LAI than the mean of the spots that were sampled by the SunScan S11 or the LI-COR 2200C. Indeed, some single readings of these two instruments were rather high (close to LAI_{DHT}), while the mean of the randomly selected samples was lower. Higher values (close to LAI_{DHT}) were noted during those measurements.

Note that the vegetation is not distributed homogeneous across the entire grassland. Patches close to the tower used to have a higher vegetation than other patches further away. Our efforts to determine the LAI with remote sensing data from a drone were not successful. The best possible estimation that we can give is that the LAI-Value is between 3.5 and 4.2 because this is the range given by the best working methods (LAI_{DHT}, LAI_{S11}, LAI_{LIC}).

Tab 5: Mean and standard deviation of the different LAI methods. Sentinel 2 data with calculation by Fan et. al. (2019)

Method	**Mean (footprint area)**	**Standard deviation**
LAI_{RS2}	3.0	0.20
LAI_{DHT}	4.2	NA
LAI_{S11}	3.6	0.35
LAI_{LIC}	3.5	0.35
LAI_{P05}	0.9	0.10

IV. Evaporation - Transpiration

We used the standardised equations of Penman (Eq. 13) and Penman-Monteith (Eq. 14) to quantify evapotranspiration (ET), the sum of evaporation and transpiration of plants. In addition, we utilized the different LAIs which we measured to quantify ET via different calculations.

IV.I. Comparison of Methods

The equations utilised to determine ET consist of common, as well as different coefficients, which are displayed in Tab. 6, Tab. 7 and Tab. 8.

IV.I.II Penman and Penman-Monteith

The purpose of the Penman equation (Penman 1963) is to determine the potential (maximum possible) evapotranspiration (PET):

$$\boldsymbol{Eq.13}: \quad \boldsymbol{PET = 0.086 * \frac{\delta}{\delta+\gamma} * \frac{Q_s - B}{L} + \frac{\gamma}{\gamma+\delta} * f(U) * \frac{e^* - e}{L}}$$

Tab. 6: Variables used in the Penman-Equation

Formula Symbol	Explanation	Unit	Source
Δ	Slope of the vapour pressure temperature relationship	[hPa K^{-1}]	Calculated from measurements
γ	Psychrometric constant	[hPa K^{-1}]	Constant (= 0.667)
Q_s	Net radiation	[W m^{-1}]	Calculated from measurements
B	Soil heat flux	[W m^{-1}]	Measurement
f(U)	Transfer coefficient for water vapour	-	Calculated from measurements
e*	Saturation water vapour pressure	[hPa]	Calculated from measurements
e	Current water vapour pressure	[hPa]	Calculated from measurements
L	Evaporation energy of water	[MJ kg^{-1}]	Constant (= 2.5)

In contrast, the Penman-Monteith equation (Allen et al. 1998) yields an approximation of the net evapotranspiration (ET) or current evapotranspiration:

$$\boldsymbol{Eq.14}: \quad \boldsymbol{ET = \frac{\delta * (Q_s - B) + \rho * c_p * \frac{e^* - e}{r_a}}{L * (\delta + \gamma * (1 + \frac{r_s}{r_a})}}$$

Tab. 7: Variables used in the Penman-Monteith-Equation

Formula Symbol	Explanation	Unit	Source
Δ	Slope of the vapour pressure temperature relationship	[hPa K^{-1}]	Calculated from measurements
γ	Psychrometric constant	[hPa K^{-1}]	Constant (= 0.667)
Q_s	Net radiation	[W m^{-2}]	Calculated from measurements
B	Soil heat flux	[W m^{-2}]	Measurement
L	Evaporation energy of water	[J kg^{-1}]	Constant (= 2500000)
e*	Saturation water vapour pressure	[hPa]	Calculated from measurements
e	Current water vapour pressure	[hPa]	Calculated from measurements
ρ	Mean air density at constant pressure	[kg m^{-3}]	Constant (= 1.2041)
c_p	Specific heat of the air	[MJ kg^{-1} K^{-1}]	Constant (= 1005)
r_a	Aerodynamic resistance	[s m^{-1}]	Calculated from measurements
r_s	(Bulk) Surface resistance	[s m^{-1}]	Calculated from measurements

In order to calculate the aerodynamic resistance r_a (Eq. 15) we used the following formula (Allen et al. 1998):

$$\boldsymbol{Eq.15}: \quad \boldsymbol{r_a = \frac{(\log(\frac{(z_w - d)}{z_{ow}}) * \log(\frac{(z_h - d)}{z_{oh}}))}{K^2 * U}}$$

For the calculation of the (bulk) surface resistance r_s we used this formula (Allen et al. 1998):

$$\textbf{Eq. 16:} \quad rs = \frac{rl}{LAI}$$

Tab. 8: Variables used to calculate the aerodynamic resistance r_a and the (bulk) surface resistance r_s

Formula Symbol	Explanation	Unit	Source
z_w	Height of wind measurements	[m]	Measurement (= 1.95)
z_{ow}	Zero plane displacement height	[m]	Calculated (= 0.123*d)
z_h	Height of temperature and humidity measurements	[m]	Measurement (= 1.95)
z_{oh}	Roughness length governing transfer of heat and vapour	[m]	Calculated (= 0.1* z_{ow})
d	Vegetation height	[m]	Measurement
K	Von Karman's constant	-	Constant (= 0.4)
U	Wind speed at height of wind measurement (zW)	[m s^{-1}]	Measurements
r_l	Stomatal resistance	[s m^{-1}]	Constant (= 100)
LAI	Leaf Area Index (for each detection method)	-	Calculated from Measurements

IV.I.II.I Results and Discussion

As shown in Eq. 16, the LAI is an important coefficient within the Penman-Monteith equation. The following LAIs were used in this equation to calculate ET: (i) LAI_{DHT}, (ii) LAI_{S11}, (iii) LAI_{LIC}, (iv) LAI_{RS2}, and (v) LAI_{P05}. The values for ET were named after the corresponding method to determine the LAI (e.g. ET_{DHT}). Another result for ET was processed directly by the EddyPro software ($ET_{EddyPro}$). The comparison of all methods used is displayed in Tab. 9, which also includes the results for the Penman equation (ET_{Penman}). Note that ET_{Penman} displays the PET.

We compared the results of half-hourly ET and PET for period 1 (Fig. 8) and of period 2 (Fig. 9). The data for Penman-Monteith is the result of ET_{S11}.

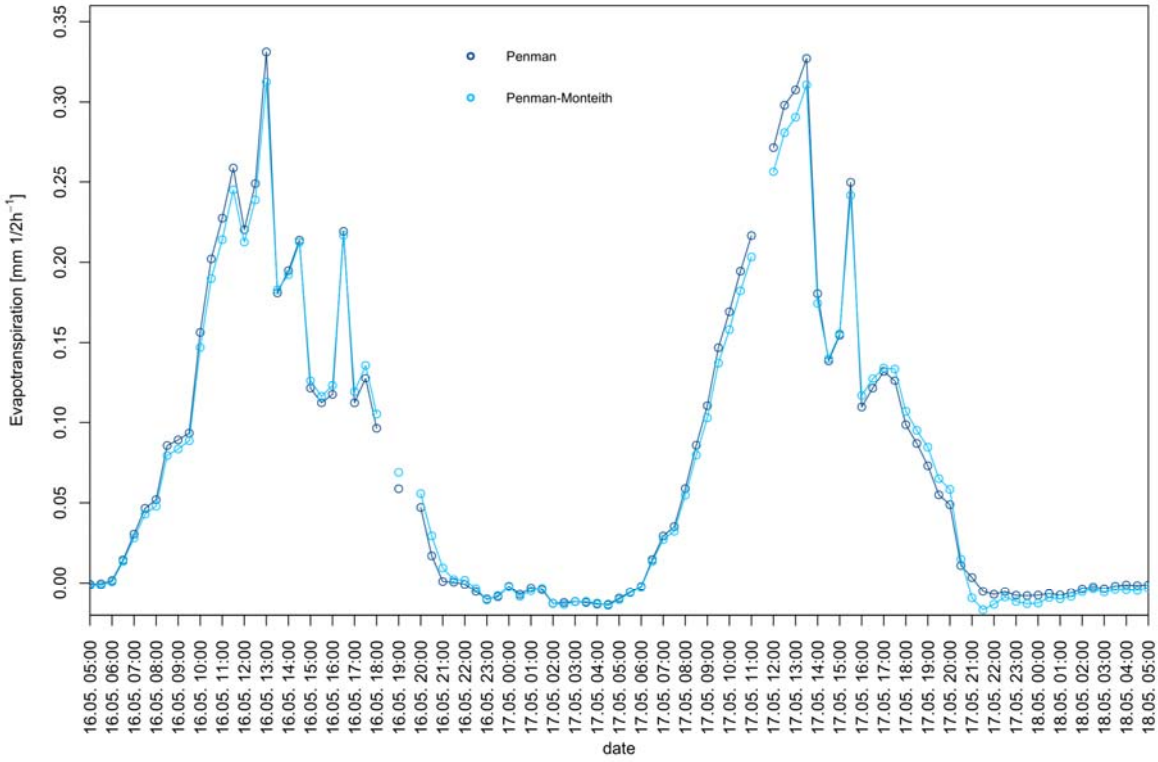

Fig. 8: Comparison of the results of the Penman and the Penman-Monteith approaches for period 1

On May 16th at 13:00 hrs the maximum PET was found 0.33 mm $(30\ min)^{-1}$ within period 1 (Fig. 8). The minimum PET was -0.01 mm $(30\ min)^{-1}$ on May 17th at 04:30 hrs. In comparison, the maximum ET was 0.31 mm $(30\ min)^{-1}$ on May 16th 13:00 hrs, while the lowest ET of -0.02 mm $(30\ min)^{-1}$ was found on May 17th 21:30 hrs.

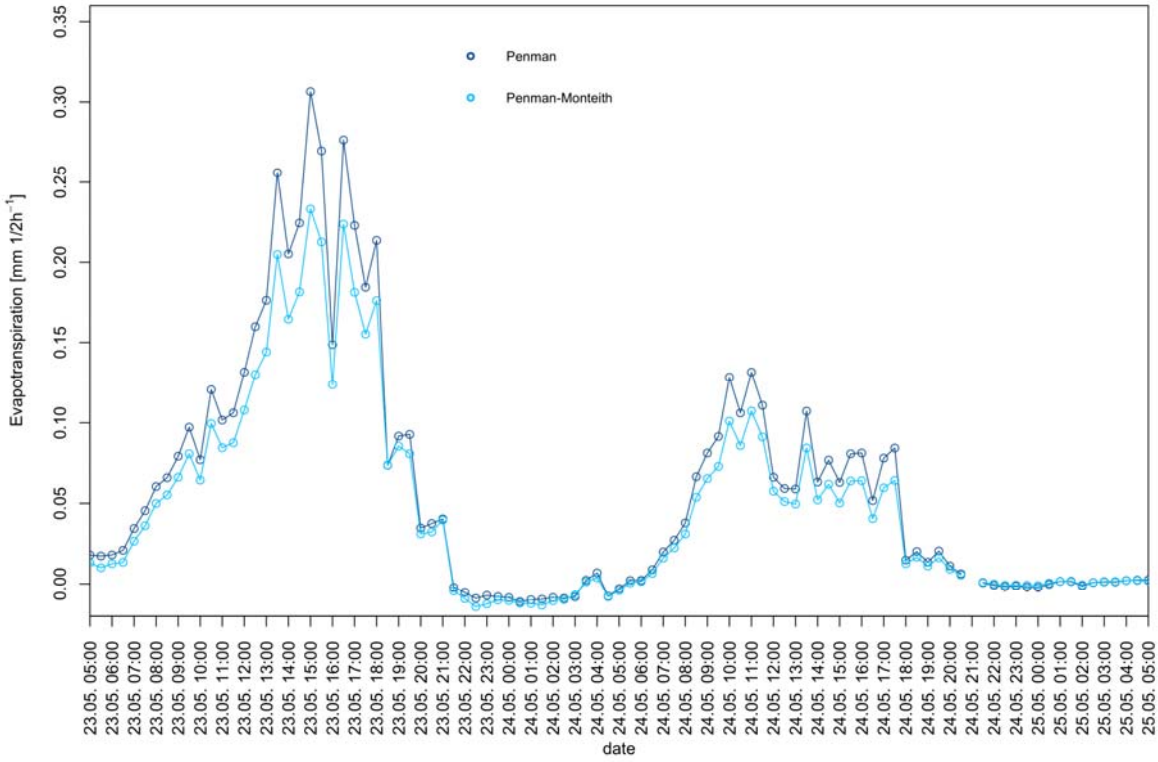

Fig. 9: Comparison of the results of the Penman and the Penman-Monteith approaches for period 2

The maximum PET within investigation period two was 0.31 mm (30 min)$^{-1}$ on May 23rd 15:00 hrs, while the minimum of -0.01 mm (30 min)$^{-1}$ was found on May 24th 00:30 hrs. The maximum ET was on May 23rd at 15:00 hrs exhibiting 0.29 mm (30 min)$^{-1}$ (Fig. 9). The minimum was found on May 24th at 01:00 hrs with -0.01 mm (30 min)$^{-1}$.

The maxima occurred between 13:00 hrs and 15:00 hrs. Negative water vapour fluxes occurred at night (see Ch. IV.III. – Dew, below).

Compared to the other days, ET and PET are lowest on May 24th. The low values for ET and PET coincide with a rain event and a cloudy sky on that day. The significantly reduced solar radiation led to an overall lower evapotranspiration on that day.

In period 1, we noticed only small differences between the results for ET and PET. In period two, the results for PET clearly exceeded the results for ET. The PET is expected to be higher than ET since the equation describes the maximum ET possible. Results for ET calculated with the Penman-Monteith equation can yet exceed PET. This phenomenon mainly occurs under water saturated conditions. In the Penman equation soil water is not considered. In the Penman-Monteith equation, soil water is implicated through r_s, since the parameter is related to soil moisture and stomatal conductance of different vegetation types (Verhoef/Egea 2014; Westerhoff 2015)

IV.I.II Comparison of LAI detection methods within the Penman-Monteith equation

In order to compare the ET of different vegetations with each other, the Food and Agriculture Organization of the United Nations (FAO) developed a formula to determine the ET of a reference surface. The reference surface is a grassland with 12 cm height and includes defined terms for r_a and r_s (Eq. 17). The equation can be adjusted to the local vegetation, which makes the ET comparable throughout different climate zones and vegetation types (Allen et al. 1998). The equation was used to determine the ET of the reference surface (ET_{REF}). In comparison, the vegetation height of the study site was at 36 cm.

$$\textbf{Eq. 17:} \quad ET_{act} = \frac{\delta * (Q_s - B) + \rho * c_p * \frac{e^* - e}{208/U}}{L * (\delta + \gamma * (1 + \frac{70}{208/U})}$$

Fig. 10 compares ET rates in period 2 (23rd May). The results were calculated for the half-hourly ET values for ET_{DHT}, ET_{S11}, ET_{RS2} and ET_{REF}. Since the LAI_{S11} and LAI_{LIC} differ by only 0.1 (Tab. 5), ET_{LIC} was excluded from the graphic. The results for ET_{LIC} are almost identical to those of ET_{S11}.

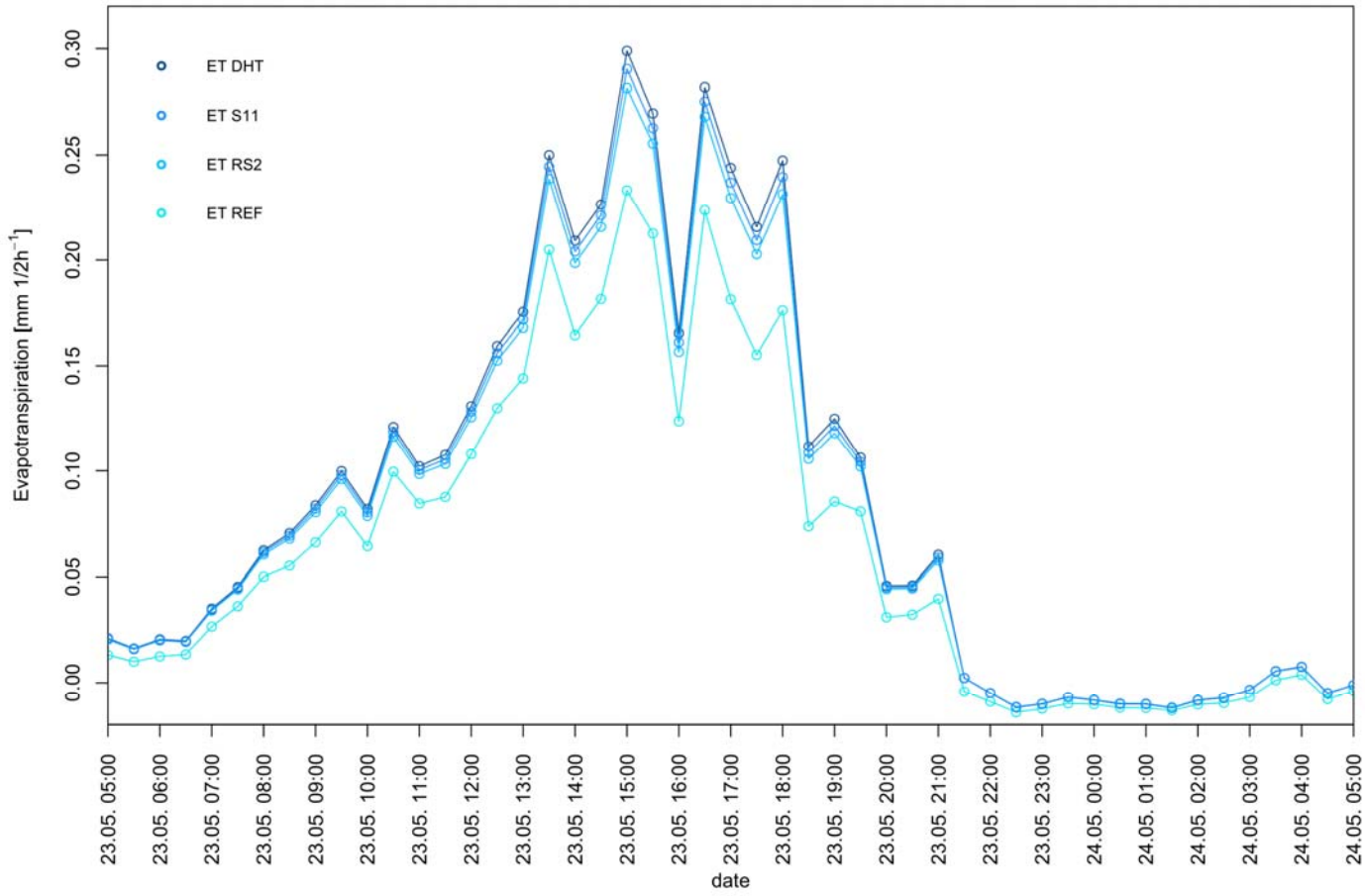

Fig. 10: ET as calculated with the Penman-Monteith equation using different methods (period 2)

The maximum ET was estimated for ET_{DHT} with 4.22 mm d^{-1} (Tab. 9). The lowest ET was estimated for ET_{REF} with 3.22 mm d^{-1}. The outcome suggests that the results of Eq. 14 are strongly influenced by the LAI coefficient.

IV.II. Sum of Evapotranspiration per Day

Daily summed up ET values were calculated with different LAI (Tab. 9). The sums contain 24 hours of data from 05:00 hrs on the starting days (May 16th and 23rd, respectively) to 05:00 hrs on the ending days (May 18th and 25th, respectively).

The daily sums of ET vary moderately between the methods. While $ET_{EddyPro}$ yields maximum daily sums of 4.53 mm d^{-1}, the minimum daily sum of ET was calculated to be 1.11 mm d^{-1} using the Pyranometer approach.

In general, the values for the Pyranometer approach are on average the lowest (mean = 2.40 mm d^{-1}) in comparison to the other methods while EddyPro results in the highest on average values (mean = 3.45 mm d^{-1}).

Tab. 9: Daily Sums of evapotranspiration for the two time periods in [mm d^{-1}]

date	$ET_{EddyPro}$	ET_{Penman}	ET_{DHT}	ET_{LIC}	ET_{S11}	ET_{REF}	ET_{P05}	ET_{RS2}
16.05.	3.84	3.65	3.68	3.62	3.62	2.99	2.68	3.54
17.05.	4.29	3.71	3.84	3.59	3.59	3.08	2.84	3.53
23.05.	4.53	3.98	4.22	4.12	4.13	3.22	2.89	4.02
24.05.	1.15	1.70	1.77	1.73	1.73	1.34	1.21	1.69

An effort for standardisation by the American Society of Civil Engineers (ASCE) was made to find a reference value for global comparison. A study in accordance to those efforts by Itenfisu et al. (2003) quantifies ET rates calculated by the Penman-Monteith method on experimental grassland plots in the magnitudes of 2.78 to 8.54 mm d^{-1} (mean = 5.66 mm d^{-1}). They further state that on average the Penman method yields PET rates 7.2 % higher than the Penman-Monteith method.

Daily sums of ET of our study calculated using all approaches are generally lower than the mean of the interval of ET rates found by Itenfisu et al. (2003). The ratio of PET calculated with the Penman approach to the values of ET via the Penman-Monteith approach lies at 23 % and is significantly higher than the value described by Itenfisu et al. (2003).

We conclude that ET rates were much lower during our periods of investigation compared to other studies. As mentioned in Chapter I, the wind speeds during our measurement period were unusually low. There is a direct dependency of evapotranspiration to a consistent air flux (Allen et al. 1998). Note that the Penman and Penman-Monteith equations include the wind speed in their calculations. Overall, this could cause reduced water vapour fluxes even over water-saturated grassland as we had around our measurement site.

IV.III. Dew

Negative ET indicates the formation of dew. Fall of dew means that no water evaporates near the ground but condenses in the area of the footprint. This phenomenon was observed over both periods at night between 22:00 hrs and 06:00 hrs. Fall of dew was indicated by all methods applied for calculating ET.

The formation of dew during the night of May 16th to May 17th (period 1) is shown in Fig. 11, regarding $ET_{EddyPro}$, ET_{S11} and ET_{Penman}. The result suggests that dew was formed at the study site.

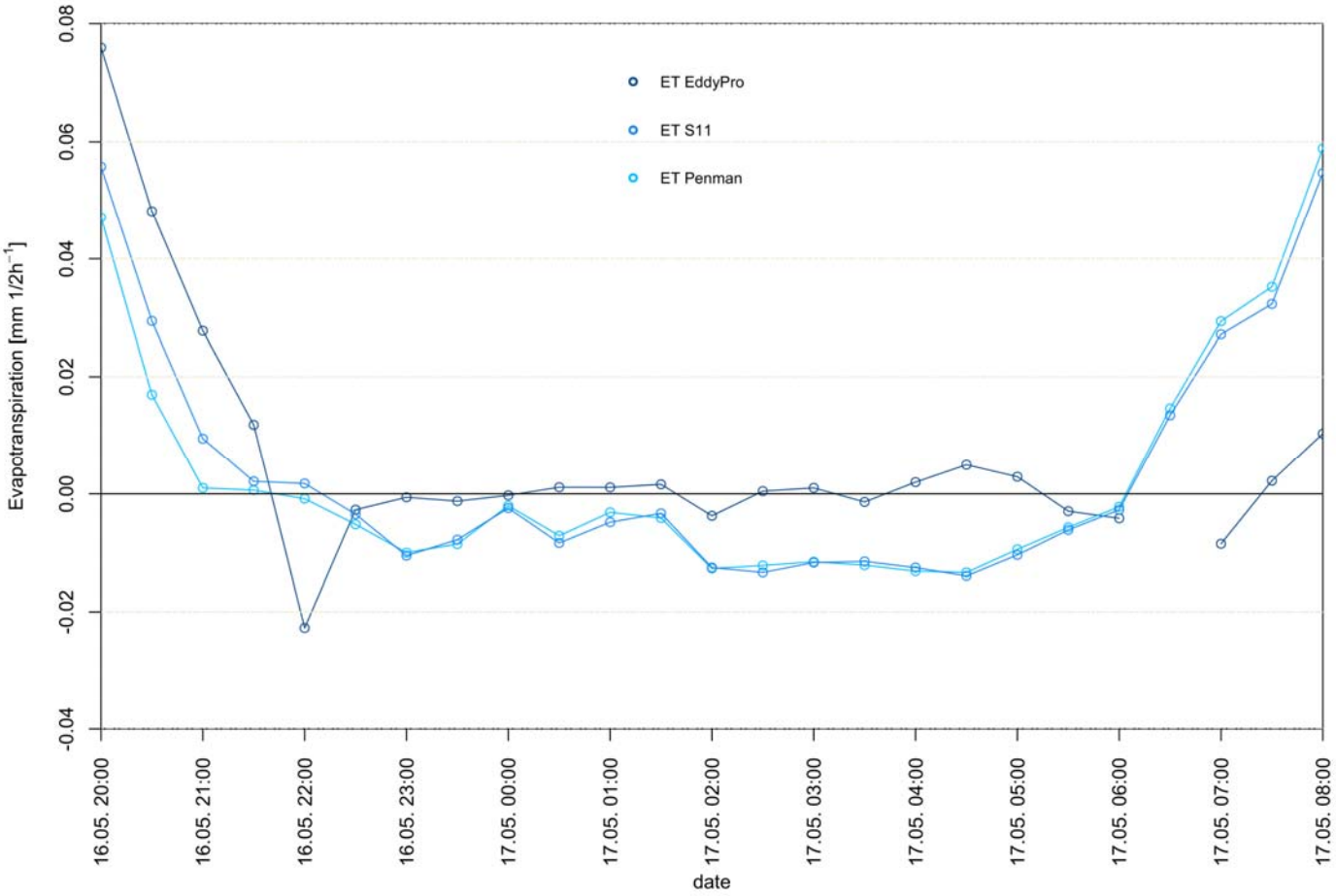

Fig. 11: Negative ET event of May 16th, 20:00 hrs until May 17th, 08:00 hrs (period 1) calculated with different methods. The black line marks zero, which indicated the transition between evapotranspiration and the formation of dew

The highest result for dew was reached by ET_{Penman} which is almost equal to ET_{S11} (Tab. 10). The result for $ET_{EddyPro}$ was the lowest. We noted that $ET_{EddyPro}$ reached the highest values for positive ET and the lowest values for negative ET.

Tab. 10: Sums of negative ET between 22:00 hrs (May 16th) and 06:00 hrs (May 17th) in [mm]

date	ET_{S11}	ET_{Penman}	$ET_{EddyPro}$
17.05.2020	-0.132	-0.133	-0.039

V. Wind statistics and friction velocity

The wind has an influence on the footprint area as well as on the flux measurements (Ch. II). In this chapter, wind speed and friction velocity during the measuring period are analysed and set into context regarding Ch. IV.

V.I. Distribution of wind speeds

Fig. 12 shows the distribution of the measured wind speeds for the whole measuring period. The histogram is based on 710 data points of 30 min means and has a median of 1.02 m s^{-1} (red vertical line). The density distribution is not symmetric as the frequency of measured wind speed phases out at higher wind speeds.

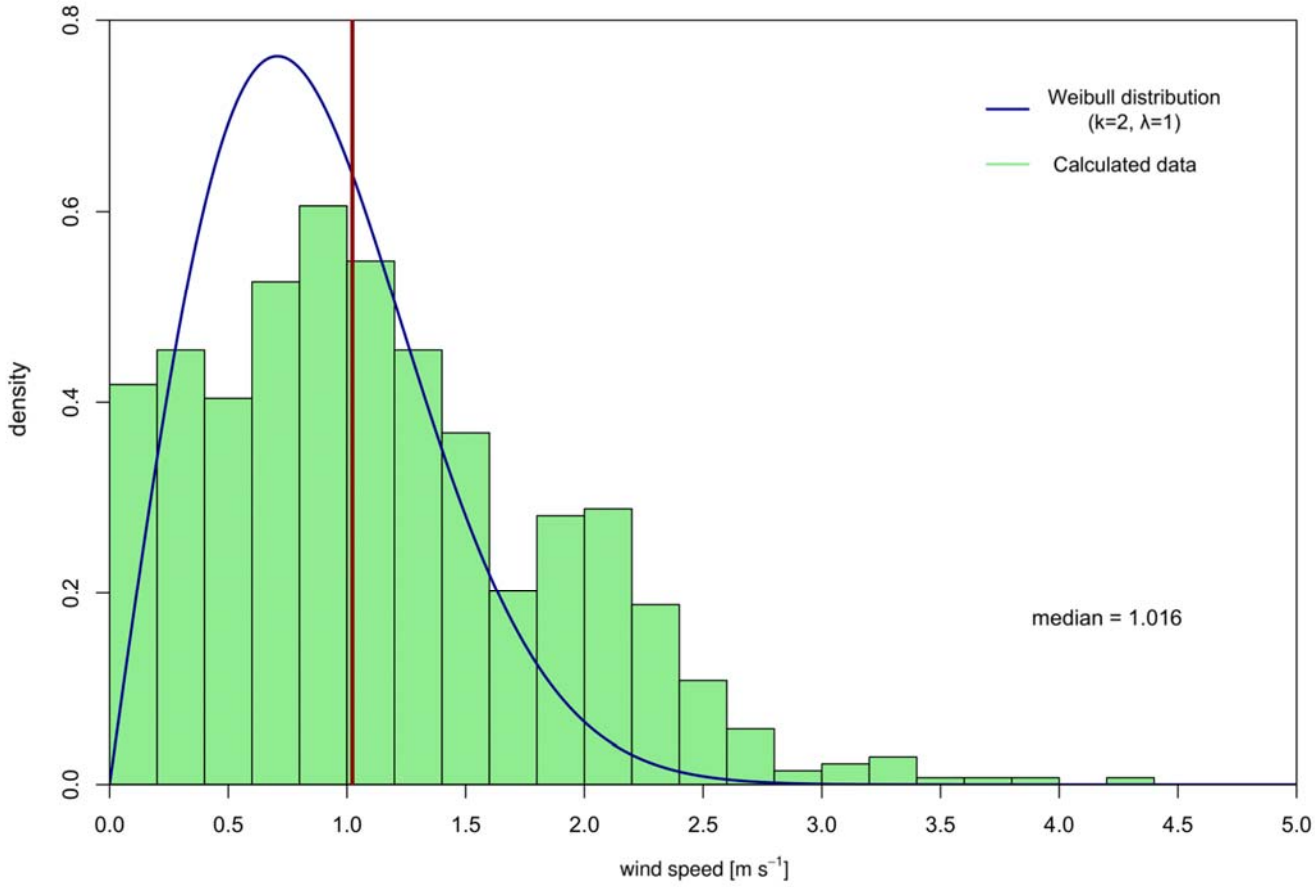

Fig. 12: Distribution of wind speeds (whole measuring period) and a fitted Weibull distribution (k=2, λ=2)

Various types of distributions may be used to approximate wind speed statistics. One of the commonly used models is the Weibull distribution. It can be fitted with the shape parameter k and the scale parameter λ or C. The effects of different shape parameters on the Weibull distribution are shown in Fig. 13.

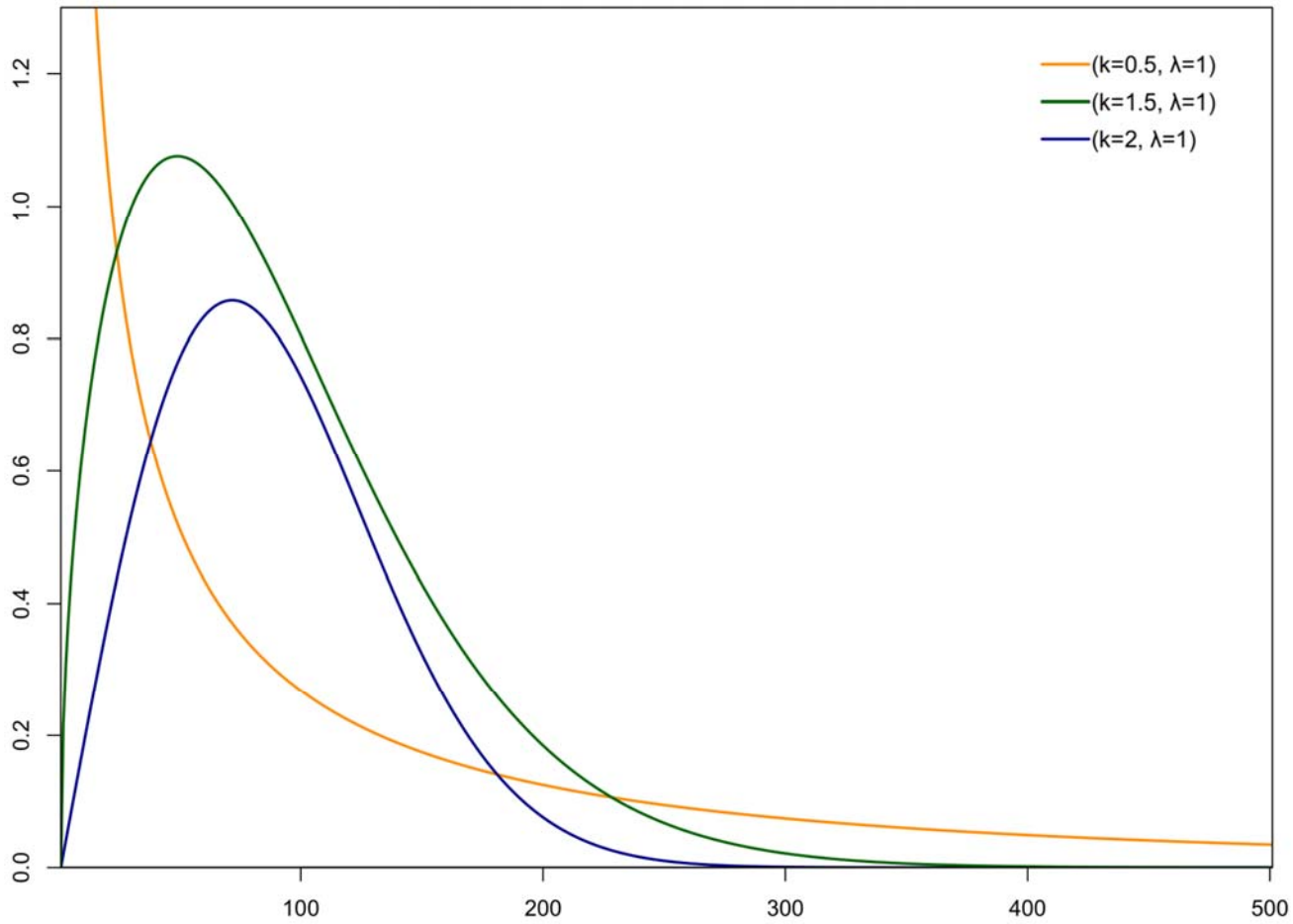

Fig. 13: Weibull distributions with different shape parameters (0.5, 1.5, 2)

Those parameters can be fitted with numerical methods (Guenoukpati et al. 2020). It is, for example, helpful to assess a location's potential for the use of wind energy. Despite deviations of our wind speed statistics from the adjusted Weibull model (Fig. 12), we assess the Weibull distribution with a shape parameter k = 2 and a scale parameter λ = 1 to be a good fit for the wind speed distribution at our site. Presumably, a larger data set covering a larger variety of weather conditions would lead to an even better agreement between the measured and modelled wind speed statistics.

V.II. Comparison of wind speed and friction velocity

Fig. 14 shows the wind speed and friction velocity over a period of six days. Both wind speed and friction velocity show pronounced daily variations. They increase in the mornings reach their maxima in the early afternoons and have their minima in the early mornings. This pattern occurs on every single day of the experimental period.

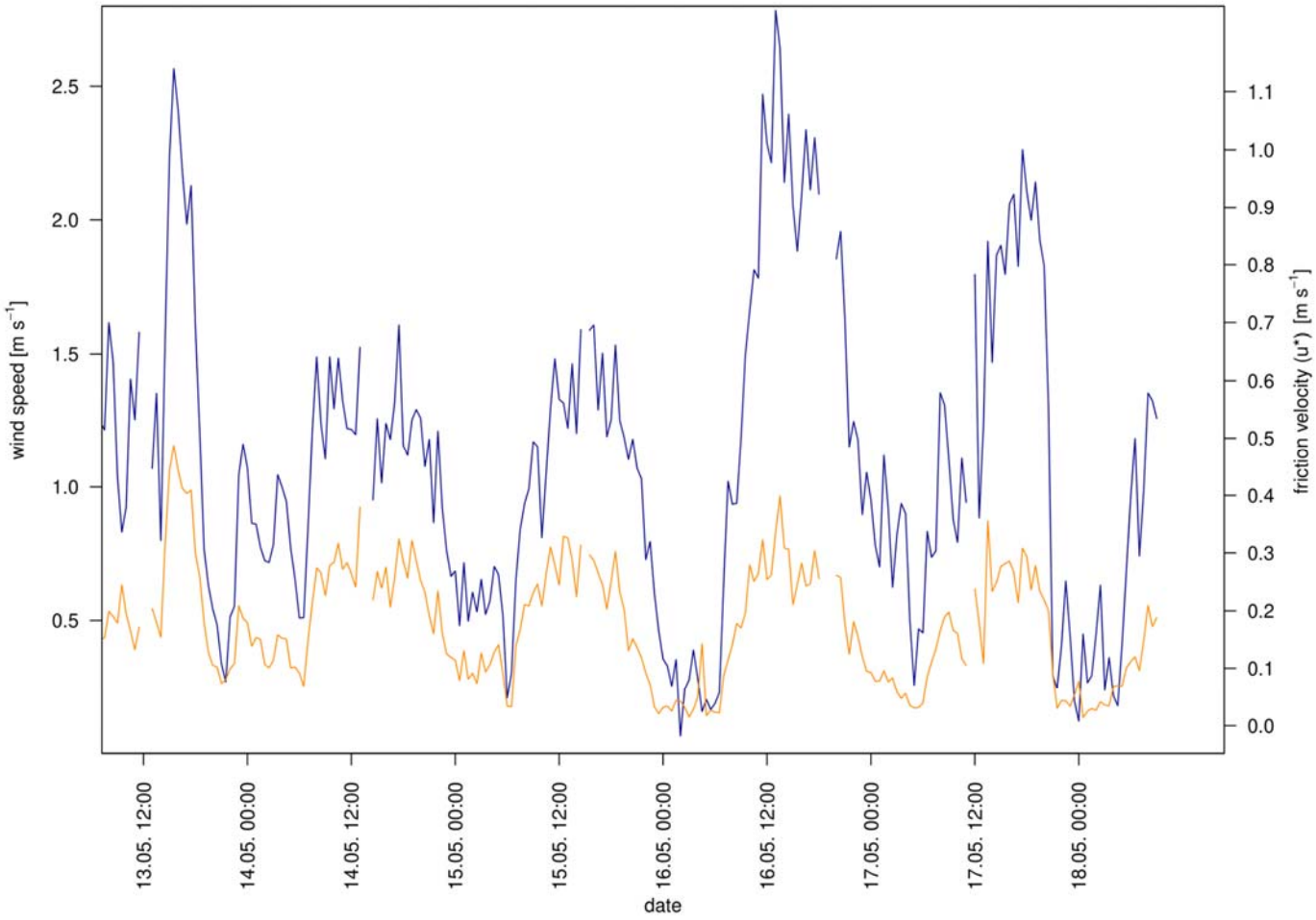

Fig. 14: Wind speed (y-axis 1) and calculated friction velocities (y-axis 2) on the measuring site from the 13th to the 18th of May 2020

The observed pattern is apparently caused by thermal turbulence occurring during the hot summer days of our campaign. The respective turbulence elements grow during the day and contain updrafts and downdrafts of air parcels. One of the consequences are compensating horizontal winds, which increase during the days. During the nights, after the solar radiation as a driver for turbulence dropped to zero, the turbulence elements and thus the horizontal winds decrease drastically (Deutscher Wetterdienst 2018). Along with the horizontal wind speed, the friction velocity shows synchronous increases and decreases. This is due to the fact that higher wind speeds lead to a higher shear stress. Our measurements took place near the ground at 2 m height. That makes friction velocities highly dependent on the surface's roughness. Both factors, the surface's roughness and the wind speed therefore affect the friction velocity (Camuffo 2014).

Fig. 15 shows a generalized linear model of wind speed and friction velocity for the whole measuring period from May 18th to May 28th. The linear regression is described by Eq.18, the coefficient of determination is 0.78, which shows a good fit of the linear model.

$$\boldsymbol{Eq.18:} \quad \boldsymbol{u^* = U * 0.135 + 0.031}$$

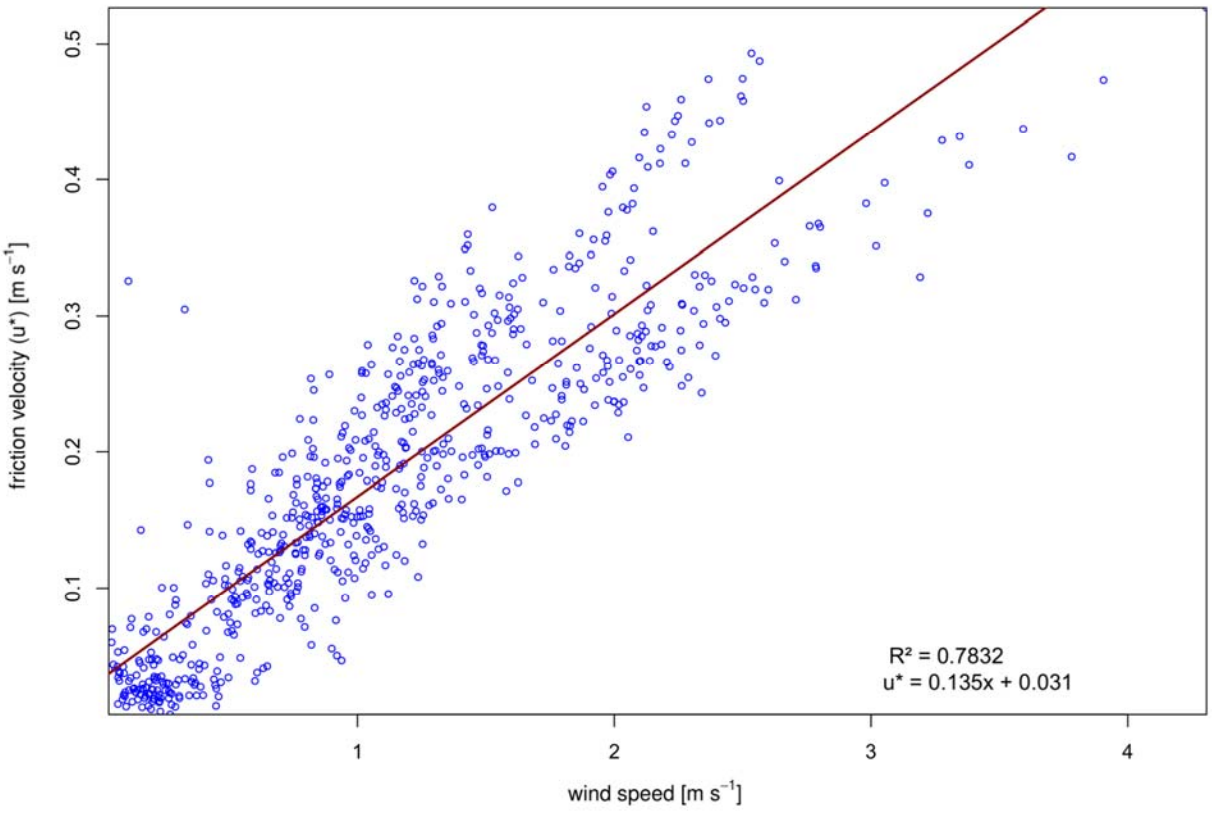

Fig. 15: Scatter plot and generalized linear model (GLM) of wind speed and friction velocity

Basically, the friction velocity can be predicted from the measured wind speed by using equation 18. The linear model's slope (0.135) can also be an estimator of the surface's roughness length. Values closer to 1 refer to a higher, while values closer to 0 refer to lower roughness length, respectively more accurate values can be calculated with Eq. 19 (Foken 2006). The roughness length (z_0) is defined by the measuring height, the mean wind speed, the friction velocity and the Karmann constant (ka). Inserting our calculated values shows the following results:

$$\boldsymbol{Eq.19:} \quad \boldsymbol{z_0 = z * e^{-U* \frac{ka}{u^*}} = 2\,[m] * e^{-1.016* \frac{0.4}{0.135}} = 0.0985\,[m]}$$

The calculated roughness length of 0.0985 m is based on the median of the wind speeds. Thus, the calculated value is not able to express the changes of the vegetation height during the measuring period. It just gives a rough understanding of the surface properties.

As data points are not distributed evenly, the statistical power for a prediction of u* decreases for wind speeds over 2 m s^{-1}. This is a common phenomenon of wind speed statistics because the distribution of wind speeds does not follow a normal distribution (Fig. 12).

V.III. Impact of the roughness length on ET

The approach to determine z_0 in this chapter differs from the approach in Ch. IV to determine z_{ow} while both values describe the roughness length. In order to estimate the impact of the roughness length on ET, both values were used in the Penman-Monteith equation (Eq. 14). The value for z_0 was 0.0985 m, while the value for z_{ow} was 0.029 m. The data was equivalent to the calculation of ET_{S11}, while the values for the roughness length were replaced as described. In addition the roughness length for heat transfer z_{oh} was recalculated for both values according to the equation for z_{oh} in Ch. IV (Tab. 8). The result is displayed in Fig. 16.

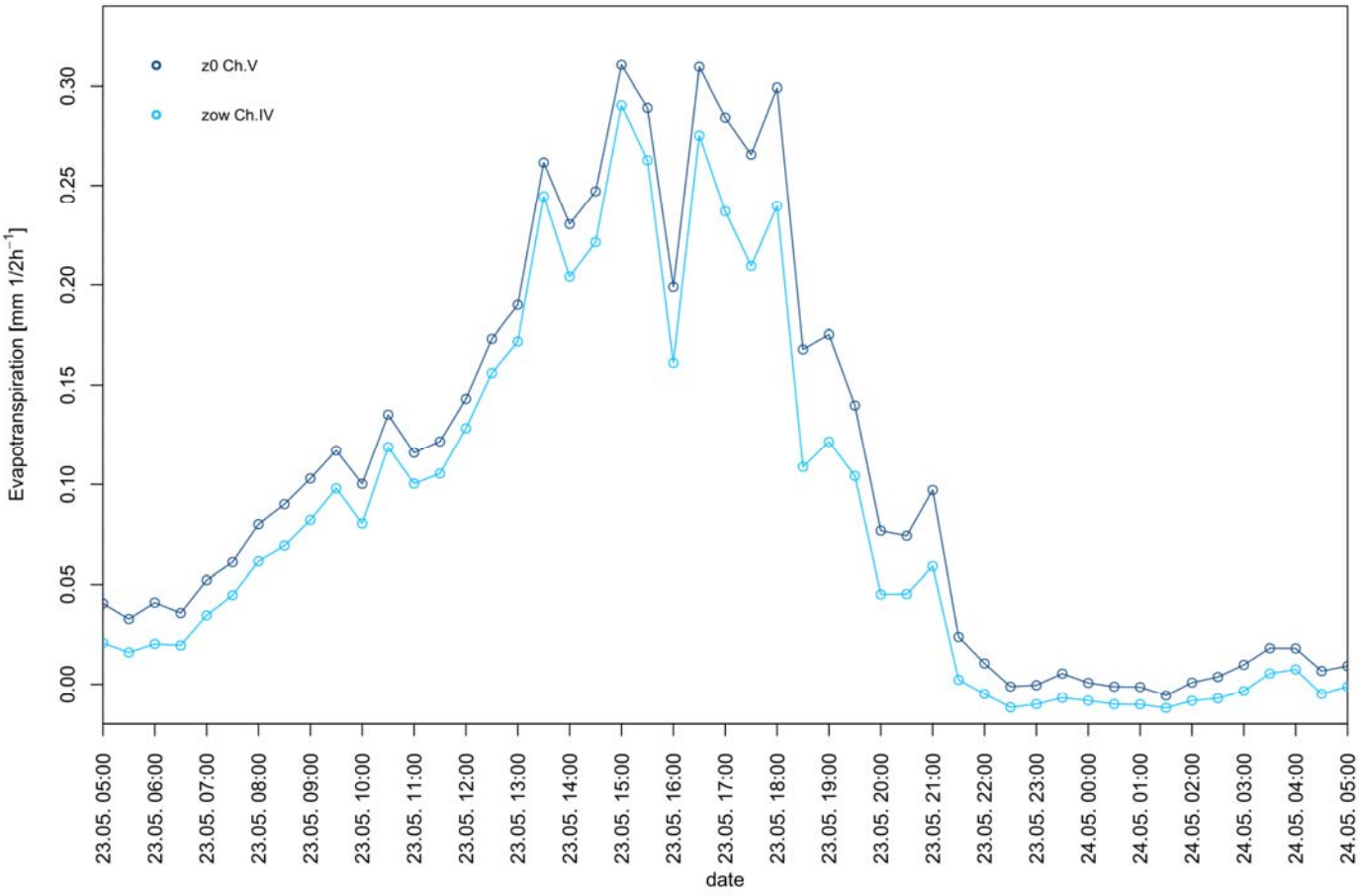

Fig. 16: Comparison of the ET using the values of z_{0w} and z_0 as mentioned in Ch. IV and Ch. V, respectively. The result is calculated for ET_{S11}

The result shows a higher ET for the calculation with z_0.

VI. CO_2 flux

Plants absorb CO_2 in their photosynthetic process. The photosynthesis mostly depends on the solar radiation and so does the vegetation-related CO_2 flux (Baumberger et al. 2019). Also, CO_2 is emitted by bacteria in the soil respiration a process, which is not related to solar radiation. During nights the plants stop the uptake of CO_2. So, the soil respiration dominates the CO_2 flux. This leads to a positive CO_2 flux at night, which means that CO_2 is mostly moved from the surface into the atmosphere. During daytime, the flux is negative, which means that the photosynthetic process is dominant, and the biosphere absorbs more CO_2 by respiration of plants than soil respiration emits.

VI.I. Quality management and Calculations

To guarantee high-quality results, steps have been taken to ensure quality assurance. After flux calculations with EddyPro, data assigned with values "-9999", which means "not enough data for flux computations ", were removed from the data set. The quality-flagging model of (Mauder/Foken 2004) was used to reject data with bad quality (flag 2). Data points that were flagged "1" or "0" were kept for further analysis. Flux data categorized as intermediate quality, which are still useable for general analysis e.g. annual budgets, are flagged "1" and flux data with high quality are flagged "0". One single spike with a value of 25 µmol CO_2 m^{-2} s^{-1} on May 18th was detected as an outlier and therefore manually excluded from further analysis. As another filter criterion u* was determined, which is a good measure of turbulence characteristics. Flux data that was calculated at atmospheric conditions with $u^* < 0.1$ m s^{-1} were marked within time series diagrams (Fig. 16 and 17). Conditions with $u^* < 0.1$ m s^{-1} typically occur during nights when turbulence is weak. Due to the methodological constraints of the eddy covariance method, such data must be interpreted with caution.

VI.II. Results

Carbon dioxide fluxes for period 1 are shown in Fig. 16. The largest positive flux in that period reaches 8.1 µmol CO_2 m^{-2} s^{-1}. The largest negative fluxes were -16.1 µmol CO_2 m^{-2} s^{-1} on May 16th and -16.5 µmol CO_2 m^{-2} s^{-1} on May 17th.

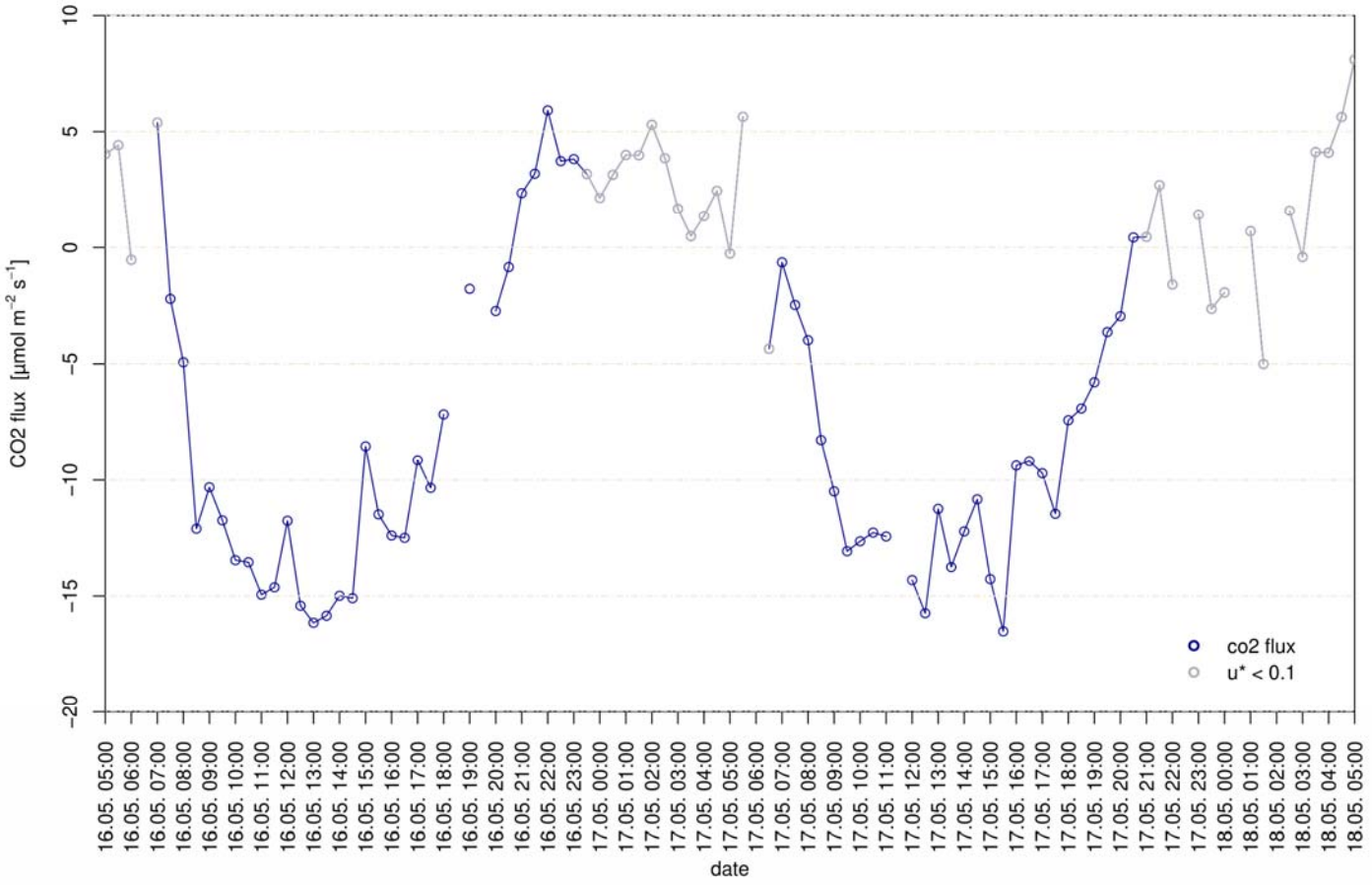

Fig. 16: CO_2 flux from 16th to 18th of May 2020 during period 1 (blue). Flux data under conditions of u* < 0.1 m s^{-1} (grey)

For period 2 (Fig. 17) the largest positive flux reaches 7.6 µmol CO_2 m^{-2} s^{-1} on May 24th and the largest negative flux -15.5 µmol CO_2 m^{-2} s^{-1} on May 23rd. Fewer negative values for the CO_2 flux on May 24th are noticeable. The minimum was -12 µmol CO_2 m^{-2} s^{-1}. Also, rain was detected on May 24th between 15:00 hrs and 19:00 hrs (Fig. 18). During this time, the negative flux (-9.7 µmol CO_2 m^{-2} s^{-1}) was smaller in comparison to the largest negative flux periods mentioned before. At the same time, the air temperature and incoming solar radiation were lower compared to the previous day (Fig. 18). During a rain event, the activities of plants such as photosynthesis are limited due to less incoming solar radiation. As a result, they absorb less CO_2. (Rannik et al. 2002) also showed that on a cloudy day photosynthetically active radiation limits the CO_2 flux the most, because it controls the mechanism of photosynthesis.

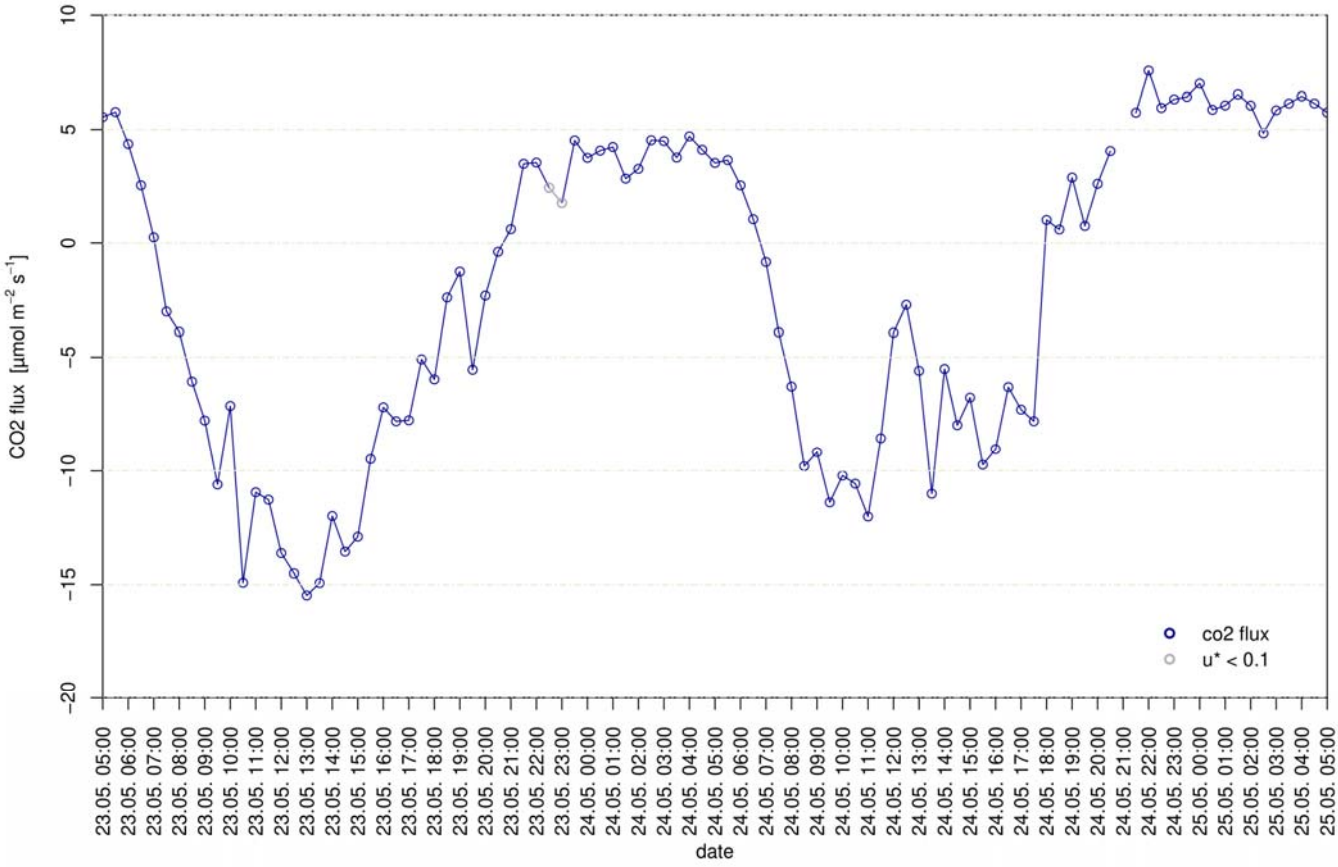

Fig. 17: CO_2 flux from 23rd to 25th of May 2020 during period 2 (blue). Flux data under conditions of u* < 0.1 m s^{-1} (grey)

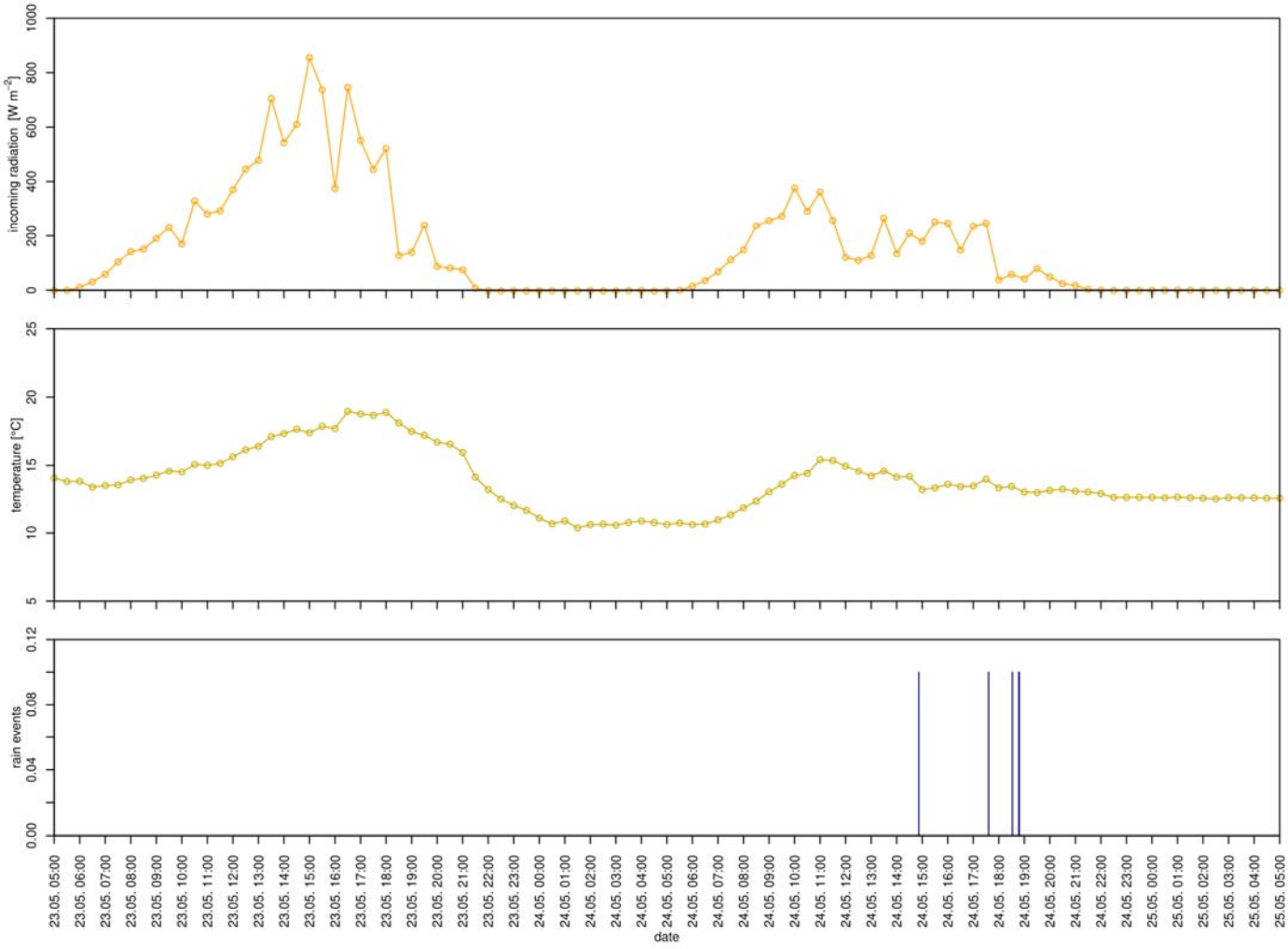

Fig. 18: Incoming solar radiation, temperature and rain from 23rd to 25th of May

VII. Conclusion and further outlook

During the field work exercise "Biosphere Atmosphere Exchange" we calculated the turbulent fluxes of CO_2, H_2O, and sensible heat of a grassland using the EC method. Furthermore, we modelled the ET rates using the Penman-Monteith equation. A central question of our study was, to what extent the LAI coefficient as part of the Penman-Monteith equation influences the calculated ET rate. Therefore, the LAI was determined by various methods.

For both measuring periods, the high-contribution source area of the footprint was located within about six metres distance to the tower. We conclude that the measurement height of the EC setup of two metres was suitable. However, taking into account the overall size of the research site, for future applications the sensors could be placed higher above the ground to increase the size of the footprint, at least for similar synoptic conditions. A larger footprint would make the flux data more representative of the whole grassland under study.

In the two measuring periods, the CO_2 fluxes (half-hour averages) ranged from 8.1 µmol CO_2 m^{-2} s^{-1} to -16.5 µmol CO_2 m^{-2} s^{-1}. The comparison of the measured CO_2 fluxes with the corresponding meteorological data confirmed that the photosynthetic activity of plants was mainly driven by the amount of incident solar radiation.

Our data also confirms that u* highly depends on wind speed. On the one hand, if wind speed and u* are known from measurements with an ultrasonic anemometer, the dependence of u* of the wind speed can be described with a generalized linear model. Its coefficient of determination is 0.78. On the other hand, the roughness length of the sites surrounding surface can be estimated from the ultrasonic anemometer data.

We compared a total of six different methods to define the LAI of the grassland under investigation. Our results show that the methods differ strongly in their accuracy and spatial representativeness.

Possible sources of error when determining the LAI directly in the field encountered within this study were random errors such as the reading inaccuracy and the heterogeneity of the vegetation. The four methods for determining the LAI with specific instrumentation (LAI-meters) are well suited for areas smaller than 400 m^2. The two sensors SunScan S11 and Licor-2200-C yielded the best and most reliable results. The averaged LAI values of the two instruments are 3.56 and 3.54. For larger areas we recommend the remote sensing methods, especially Sentinel 2, to determine the LAI. Our efforts to determine the LAI with remote sensing data captured by a drone were not successful.

A comparison of PET and ET results showed that ET can exceed PET during water-saturated soil conditions. The Penman-Monteith equation, uses the LAI as an important coefficient. A comparison of the ET rates calculated with the different methods for determining the LAI was meant to clarify the influence of the LAI on the result of the Penman-Monteith equation. Our results indicate that the ET rates are moderately influenced by the LAI. The difference in ET on May 23rd differs by 68 % between the results based on LAI_{DHT} and LAI_{P05}. Different approaches to determine roughness length also showed an influence on the results for ET.

On May 23rd the overall highest ET was at 4.52 mm d^{-1}, while on May 24th, the overall lowest ET was at 1.11 mm d^{-1}.

Furthermore, the phenomenon of dew formation was observed during the nights between 22:00 hrs and 06:00 hrs. All methods for calculating ET indicated dew formation in the form of negative ET.

An important finding from the project is that the quality of the data also determines the significance of the results. Furthermore, when carrying out, evaluating, and comparing different methods for determining relevant measured variables, it is crucial to identify potential sources of error and keep them as low as possible. Without a sufficient description of the uncertainty, measured and modelled values of LAI, ET, and PET should always be treated and interpreted with caution.

VIII. Acknowledgements

We acknowledge J. Binder and J. Lehmann from the Remote Sensing and Spatial Modelling research group of the University of Münster for supporting our study by deploying the UAV and providing laser scanner data and infrared aerial images of the study area.

IX. References

Allen, R. G.; **Pereira, L. S.**; **Raes, D.**; **Smith, M.** (1998): Crop evapotranspiration. Guidelines for computing crop water requirements (FAO irrigation and drainage paper, 56). Rome.

Baumberger, M.; **Müller, M.**; **Paas**; **B.**; **Klemm**; **O.** (2019): Short wave radiation: Influence on carbon dioxide and water va-pour flux measured by eddy covariance over a temperate lowland grassland.

Bernstein, L.; **Bosch, P.**; **Canziani, O.**; **Chen, Z.**; **Christ, R.**; **Davidson, O.**; **Hare, W.**; **Huq, S.**; **Karoly, D.**; **Kattsov, V.**; **Kundzewicz, Z.**; **Liu, J.**; **Lohmann, U.**; **Manning, M.**; **Matsuno, T.**; **Menne, B.**; **Metz, B.**; **Mirza, M.**; **Nicholls, N.**; **Nurse, L.**; **Pachauri, R.**; **Palutikof, J.**; **Parry, M.**; **Qin, D.**; **Nijavalli**; **R.**; **Reisinger, A.**; **Ren, J.**; **Riahi, K.**; **Rosenzweig, C.**; **Rusticucci, M.**; **Schneider, S.**; **Sokona, Y.**; **Solomon, S.**; **Stott, P.**; **Stouffer, R.**; **Sugiyama, T.**; **Swart, R.**; **Tirpak, D.**; **Vogel, C.**; **Yohe, G.** (2008): Climate Change 2007: Synthesis report. A report of the Intergovernmental Panel on Climate Change. Geneva: IPCC.

Burba, G. (2013): Eddy covariance method for scientific, industrial, agricultural, and regulatory applications. A field book on measuring ecosystem gas exchange and areal emission rates. Lincoln, Nebraska: LI-COR Biosciences.

Burrows, S. N.; **Gower, S. T.**; **Clayton M. K.**; **Mackay D. S.**; **Ahl, D. E.**; **Norman, J. M.**; **Diak, G.** (2002): Application of Geostatistics to Characterize Leaf Area Index (LAI) from Flux Tower to Landscape Scales Using a Cyclic Sampling Design. In: Ecosystems 5, 667–679.

Camuffo, D. (2014): Microclimate for Cultural Heritage. Conservation and Restoration of Indoor and Outdoor Monuments. Elsevier.

Danner, M.; **Locherer, M.**; **Hank, T.**; **Richter, K.** (2015): Measuring Leaf Area Index (LAI) with the LI-Cor LAI 2200C or LAI-2200 (+2200Clear Kit) – theory, measurement, problems, interpretation. GFZ Data Services.

Deutscher Wetterdienst, Abteilung Flugmeteorologie (2018): Was sie schon immer über Turbulenz wissen wollten, available online at <https://www.dwd.de/DE/fachnutzer/luftfahrt/download/produkte/runwaymap/02_alles_ueber_turbulenzen.pdf?__blob=publicationFile&v=3>, accessed July 04, 2020.

Eugster, W. (2010): Grenzschichtmeteorologie. Skript Frühlingssemester 2010.

Fan, L.; **Gao, Y.**; **Brück, H.**; **Bernhofer, Ch.** (2009): Investigating the relationship between NDVI and LAI in semi-arid grassland in Inner Mongolia using in-situ measurements. In: Theoretical and Applied Climatology 95 (1-2), 151–156.

Fang, H.; **Jiang, C.**; **Li, W.**; **Wei, S.**; **Baret, F.**; **Chen, J. M.**; **Garcia-Haro, J.**; **Liang, S.**; **Liu, R.**; **Myneni, R. B.**; **Pinty, B.**; **Xiao, Z.**; **Zhu, Z.** (2013): Characterization and intercomparison of global moderate resolution leaf area index (LAI) products: Analysis of climatologies and theoretical uncertainties. In: Journal of Geophysical Research: Biogeosciences 118 (2), 529–548.

Finnigan, J. (2004): The footprint concept in complex terrain. In: Agricultural and Forest Meteorology 127 (3-4), 117–129.

Foken, Thomas (2006): Angewandte Meteorologie. Mikrometeorologische Methoden. Berlin, Heidelberg: Springer-Verlag Berlin Heidelberg.

Guenoukpati, A.; **Salami, A. A.**; **Kodjo, M. K.**; **N., K.** (2020): Estimating Weibull Parameters for Wind Energy Applications using Seven Numerical Methods: Case studies of three costal sites in West Africa. In: International Journal of Renewable Energy Development 9 (2), 217–226.

Itenfisu, D.; **Elliott, R. L.**; **Allen, R. G.**; **Walter, I. A.** (2003): Comparison of Reference Evapotranspiration Calculations as Part of the ASCE Standardization Effort. In: Journal of Irrigation and Drainage Engineering 129 (6), 440–448.

Jurik, T. W.; **Briggs, G. M.**; **Gates, D. M.** (1985): A comparison of four methods for determining leaf area index in successional hardwood forests. In: Canadian Journal of Forest Research 15 (6), 1154–1158.

Kljun, N.; **Sprenger, M.**; **Schr, C.** (2001): Frontal modification and lee cyclogenesis in the Alps: A case study using the ALPEX reanalysis data set. In: Meteorology and Atmospheric Physics 78 (1-2), 89–105.
Li-Cor (2020): Tovi Data Analysis Software, available online at <https://www.licor.com/tovi/>, accessed July 11, 2020.
Mauder, M.; **Foken, T.** (2004): Documentation and Instruction Manual of the Eddy Covariance Software Package TK2.
Mauder, M.; **Foken, T.** (2011): Documentation and Instruction Manual of the Eddy-Covariance Software Package TK3, available online at <https://epub.uni-bayreuth.de/342/1/ARBERG046.pdf>, accessed July 11, 2020.
Pasqualotto, N.; **Delegido, J.**; **van Wittenberghe, S.**; **Rinaldi, M.**; **Moreno, J.** (2019): Multi-Crop Green LAI Estimation with a New Simple Sentinel-2 LAI Index (SeLI). In: Sensors (Basel, Switzerland) 19 (4).
Penman, H. L. (1963): Vegetation and hydrology. In: Quarterly Journal of the Royal Meteorological Society 89 (382), 565–566.
Rannik, Ü.; **Altimir, N.**; **Raittila, J.**; **Suni, T.**; **Gaman, A.**; **Hussein, T.**; **Hölttä, T.**; **Lassila, H.**; **Latokartano, M.**; **Lauri, A.**; **Natsheh, A.**; **Petäjä, T.**; **Sorjamaa, R.**; **Ylä-Mella, H.**; **Keronen, P.**; **Berninger, F.**; **Vesala, T.**; **Hari, P.**; **Kulmala, M.** (2002): Fluxes of carbon dioxide and water vapour over Scots pine forest and clearing. In: Agricultural and Forest Meteorology 111 (3), 187–202.
Schmid, H. P. (2002): Footprint modeling for vegetation atmosphere exchange studies: a review and perspective. In: Agricultural and Forest Meteorology 113 (1-4), 159–183.
Verhoef, A.; **Egea, G.** (2014): Modeling plant transpiration under limited soil water: Comparison of different plant and soil hydraulic parameterizations and preliminary implications for their use in land surface models. In: Agricultural and Forest Meteorology 191, 22–32.
Westerhoff, R. S. (2015): Using uncertainty of Penman and Penman–Monteith methods in combined satellite and ground-based evapotranspiration estimates. In: Remote Sensing of Environment 169, 102–112.